Dalton Transactions

PAPER

View Article Online
View Journal

Published on 04 July 2016. Downloaded by Monash University on 19/07/2016 03:34:49.

Cite this: DOI: 10.1039/c6dt02548j

Near-infrared light triggered superior photocatalytic activity from MoS_2–$NaYF_4$:Yb^{3+}/Er^{3+} nanocomposites†

Manjunath Chatti, Venkata N. K. B. Adusumalli, Sagar Ganguli and Venkataramanan Mahalingam*

Received 25th June 2016,
Accepted 3rd July 2016

DOI: 10.1039/c6dt02548j

www.rsc.org/dalton

A near infrared (NIR) responsive photocatalyst, composed of a narrow band gap semiconductor (*i.e.* MoS_2) and an optical material possessing upconverting ability (*i.e.* $NaYF_4$:Yb^{3+}/Er^{3+}) has been successfully prepared *via* a simple hydrothermal method. The latter has the ability to convert NIR light into visible light while the MoS_2 uses the light to degrade organic pollutants. Upon near infrared (NIR) excitation of the MoS_2–$NaYF_4$:Yb^{3+}/Er^{3+} nanocomposites, the energy of the strong green and the red emissions along with the weak violet emissions from the $NaYF_4$:Yb^{3+}/Er^{3+} nanocrystals (NCs) is transferred to MoS_2. This results in enhanced NIR light triggered photocatalytic performance, as verified by studying the degradation of Rhodamine B (RhB) dye under 980 nm laser excitation. The strong photocatalytic activity of MoS_2–$NaYF_4$:Yb^{3+}/Er^{3+} composites is attributed to the layered nature of the photocatalyst which leads to the efficient separation of photogenerated carriers (electron–hole pairs) and excellent upconversion properties of $NaYF_4$:Yb^{3+}/Er^{3+} NCs. The study also shows the importance of the composite formation, as the physical mixture leads to only very low photocatalytic activity. Our results can be helpful in the structural design and development of high-performance photocatalysts.

Introduction

With increased developments in science and technology, air and water pollution have become major concerns to society. In an effort to control the pollution, an environmentally friendly photocatalysis technique is applied to the degradation of organic pollutants in air and water. In the past, considerable attention has been paid to semiconductor-based photocatalysis for water treatment because of its efficient conversion of organic pollutants to environmentally friendly by-products.[1–4] In general, the overall photocatalytic performance of semiconductors is decided by three main factors: (1) the adsorption ability of the photocatalyst, (2) the separation and migration rate of the photogenerated carriers (holes and electrons) to the surface of the catalyst, and (3) photoabsorption ability in the available light energy region.[5] Desirable photocatalysts are expected to satisfy these factors. With respect to the above factors, traditional photocatalysts, such as TiO_2 and ZnO with a wide band gap, can exhibit high photocatalytic activity only under ultraviolet light irradiation. This significantly limits their practical applications[6–8] as it is well known that UV light covers only about 5% of the solar spectrum. On the other hand, visible light and near-infrared (NIR) light occupy a significant portion of the solar spectrum: 49% and 46%, respectively.[9] Therefore, the development of a photocatalyst for efficient sunlight harvesting is a challenge.[10] Furthermore, smaller sphere-shaped nanoparticles are generally preferred as photocatalysts due to their higher specific surface area. But the latter's photocatalytic activity is significantly affected by a higher electron–hole recombination rate.[11] Recent studies have demonstrated that the geometry of a photocatalyst has a significant effect on the photocatalytic activity.[12]

In the recent past, photocatalysis using 2D materials has attracted researchers around the world and has become an interesting research topic.[13–15] 2D layered materials possess two main intrinsic advantages which can be utilized to enhance photocatalytic efficiency. First, 2D materials maximize the surface area available per amount of material for photocatalytic reactions. Second, due to the 2D nature the distance that photogenerated carriers (electrons and holes) have to migrate will be less, thereby reducing the possible recombination of electron and hole and potentially enhancing photocatalytic performance. Among various 2D materials MoS_2 is

Department of Chemical Sciences, Indian Institute of Science Education and Research (IISER), Kolkata, Mohanpur, West Bengal, 741246, India.
E-mail: mvenkataramanan@yahoo.com; Fax: +91-33-25873020;
Tel: +91 9007603474

† Electronic supplementary information (ESI) available: FTIR spectra, lifetime, power dependent plot, energy transfer mechanism. See DOI: 10.1039/c6dt02548j

Published on 04 July 2016. Downloaded by Monash University on 19/07/2016 03:34:49.

quite interesting and widely studied. MoS_2, being an inorganic graphene analogue, consists of molybdenum atoms sandwiched between two layers of hexagonally close-packed sulfur atoms.[16–19] With a narrow band gap of 1.8 eV, MoS_2 has strong absorption in the visible region of the solar spectrum; therefore it has been investigated for photocatalytic applications.[20–24] Although there are quite a few reports on visible light photocatalysts, research efforts on NIR-driven photocatalytic activities are still in their early stages.

Recently, there have been a few reports on NIR light triggered photocatalysts developed by integrating semiconductors with upconversion (UC) nanocrystals. The latter possess the ability to convert NIR photons into visible photons.[25–37] Moreover, the long luminescence lifetimes of the lanthanide ions ensures the efficient energy transfer to semiconductors. For example, Weiping *et al.* developed NIR-driven TiO_2 and ZnO-based photocatalysts by preparing YF_3:Yb^{3+}/Tm^{3+}@TiO_2,[38] $NaYF_4$:Yb^{3+}/Tm^{3+}@TiO_2 [39] core/shell nanoparticles and $NaYF_4$:Yb^{3+}/Tm^{3+}@ZnO[40] nanocomposites, respectively. However, because of the larger band gap of these semiconductors, only a small amount of weak upconverted UV light can be harvested under NIR irradiation rather than stronger visible emissions. To our knowledge, there are only a few reports where researchers have developed composites which can harvest the upconverted visible light.[41–44] For instance, Li *et al.* have recently reported the NIR-driven photocatalytic activity of a $NaYF_4$:Yb^{3+}, Er^{3+}/CdS composite.[41] Similarly, Guo *et al.* have reported NIR-assisted photocatalysis by a $NaYF_4$:Yb^{3+},Er^{3+}/CdS/TiO_2 composite, which is able to degrade about 90% of MB in 50 hours.[42] In another piece of work, enhanced NIR-driven photocatalytic activity was observed from a β-NaYF4:Yb^{3+},Tm^{3+}/g-C_3N_4 nanocomposite.[44] Our idea is to integrate UC NCs with the layered narrow band gap semiconductor MoS_2 to efficiently utilize the upconverted visible emissions. One of the advantages of using MoS_2 is the broad absorption in the visible region, which can thus efficiently use the unconverted emissions.

In this work, we report the NIR light triggered photocatalytic activity of MoS_2–$NaYF_4$:Yb^{3+}/Er^{3+} nanocomposites prepared using a hydrothermal method. The energy of intense green and red emissions along with weak upconverted UV emission from UC NCs is efficiently transferred to the MoS_2. This results in enhanced NIR light triggered photocatalytic activity of MoS_2 which is verified by monitoring the degradation of Rhodamine B (RhB) dye. The degradation of dye occurs much faster compared to other reports in the literature. These results pave the way to the structural design of new types of NIR-active catalytic materials.

Experimental section

Chemicals and materials

Of the chemicals used in this work, yttrium oxide (Y_2O_3, 99.99%), ytterbium oxide (Yb_2O_3, 99.99%), and erbium oxide (Er_2O_3, 99.99%) were purchased from Sigma Aldrich. Adipic acid (AA) (90%), ammonium heptamolybdate, thiourea, sodium fluoride (NaF), nitric acid (HNO_3), and absolute ethanol were purchased from Merck. All the materials were used without further purification. Lanthanide nitrates were prepared by mixing appropriate amounts of the corresponding oxides with conc. HNO_3, and the residual HNO_3 was removed by evaporation.

Synthesis

Synthesis of adipic acid coated $NaYF_4$:Yb^{3+}/Er^{3+} nanocrystals. $NaYF_4$:Yb^{3+}/Er^{3+} NCs were synthesized *via* a high-temperature hydrothermal method. Briefly, $Ln(NO_3)_3$, (Ln: 78 mol% Y^{3+}, 20 mol% Yb^{3+}, 2 mol% Er^{3+}) was dissolved in 15 mL distilled water and then 15 mL ethanol were added to the aqueous solution under magnetic stirring. Then 8 mmol NaF and 4 mmol of adipic acid were added into the above solution. The mixture was stirred for about 30 minutes before being transferred to a 50 mL autoclave, sealed, and hydrothermally treated at 200 °C for 24 h. The system was naturally cooled to room temperature, and the products were deposited at the bottom of the vessel. Pure powders could be obtained by purifying the samples with ethanol several times to remove excess NaF.

Synthesis of MoS_2. MoS_2 nanosheets were synthesized *via* a hydrothermal method, similar to those previously reported. Briefly, to a beaker containing 15 mL water appropriate amounts of ammonium heptamolybdate and thiourea were added and stirred for 30 minutes. The clear solution was subsequently transferred into a Teflon-lined autoclave and heated at 220 °C for 24 h. Subsequently, the reaction system was allowed to cool to room temperature. As a final step, the product was collected by means of centrifugation, washed twice with ethanol, and once with deionized water.

Synthesis of MoS_2–$NaYF_4$:Yb^{3+}/Er^{3+} nanocomposites. A hydrothermal synthesis technique was adopted for the synthesis of MoS_2–$NaYF_4$:Yb^{3+}/Er^{3+} nanocomposites. In a typical procedure, 50 mg of MoS_2 were well dispersed in 15 mL of water *via* sonication. To the above dispersion $Ln(NO_3)_3$, (Ln: 78 mol% Y^{3+}, 20 mol% Yb^{3+}, 2 mol% Er^{3+}) were added and stirred for 30 minutes followed by addition of 15 mL of ethanol. Then 8 mmol NaF and 4 mmol of adipic acid were added into the above solution. The mixture was stirred for about 1 h, then transferred to a 50 mL autoclave, sealed, and hydrothermally treated at 200 °C for 24 h. The system was naturally cooled to room temperature, and the products deposited at the bottom of the vessel were purified with ethanol several times to remove excess NaF.

Photocatalytic activity evaluation. The photocatalytic activity of the composites was evaluated by studying the degradation of Rhodamine B (RhB) under near-infrared (NIR) light irradiation by a 980 nm diode laser source from RGB Lase LLC. In each experiment, 20 mg of sample were dispersed into a quartz vial containing 10 mL RhB solution (25 mg L^{-1}). Prior to irradiation, the suspensions were stirred in the dark for 1 hour to reach adsorption–desorption equilibrium. Subsequently, the colloidal dispersion was exposed to NIR light irradiation inside a closed black chamber with continuous

 This journal is © The Royal Society of Chemistry 2016

Published on 04 July 2016. Downloaded by Monash University on 19/07/2016 03:34:49.

magnetic stirring. At each irradiation time interval, a 1 mL aliquot of the suspension containing the photocatalyst and RhB solution was collected and centrifuged (6500 rpm, 5 minutes) to remove the photocatalyst particles in order to assess the rate of degradation photometrically. The colloidal dispersion was analyzed by a Hitachi UV-4100 UV-vis-NIR spectrophotometer, and the characteristic absorption of RhB at 554 nm was used to monitor the photocatalytic degradation. All the measurements were carried out at room temperature.

Photogenerated hydroxyl radical ($^{\bullet}OH$) detection. A 4 mM terephthalic acid (TA) solution was prepared in a 2 mM NaOH solution. To 10 mL TA solution, 20 mg of photocatalyst were added and dispersed thoroughly *via* sonication. The resulting mixture was then irradiated with a 980 nm laser and after a certain interval, 1.0 mL of suspension was collected and centrifuged. For the photoluminescence measurement, 0.5 mL of as-collected dispersion was diluted five times. The generation of 2-hydroxyterephthalic (TAOH) acid was monitored using a fluorescence spectrophotometer with an excitation wavelength of 312 nm.

Characterization techniques

The crystallinity and phase analyses of the nanomaterials were carried out using powder X-ray diffraction (PXRD) measurements using a Rigaku-Smart lab diffractometer with Cu-Kα operating at 70 kV and 35 mA at a scanning rate of 1° per minute in the range of 10–90°. The samples were completely powdered and spread evenly on a quartz slide. The morphology of the nanomaterials was characterized by scanning electron microscopy (SEM). SEM images were taken using a ZEISS (SUPRA) instrument and for this the samples dispersed in ethanol were drop cast on a silicon wafer and further coated with a thin film of gold/platinum to avoid charging effects prior to loading of the samples into the chamber. The FTIR spectra were recorded using a Perkin Elmer RX1 spectrophotometer, using a KBr disk technique operating in the range of 4000–400 cm^{-1}. For recording the FTIR spectra, 10 mg of the samples were mixed with 200 mg of KBr to make the pellets. The photoluminescence measurement was performed using a Horiba Jobin Yvon Flurolog spectrophotometer equipped with a 450 W Xe lamp. The PL lifetime measurements were performed with a Horiba Jobin Yvon Fluorolog CP machine equipped with a pulsed Xe source operating at 25 W. The upconversion emission (UC) measurements were done by exciting the dispersion of the nanocrystals using a 980 nm diode laser source from RGB Lase LLC, which was coupled with a fiber with a core diameter of 100 μm. The output signal was measured with the Horiba Jobin Yvon Flurolog spectrophotometer. BET surface area measurements were carried out by N_2 adsorption at 77.3 K using a Quantachrome Novawin2 instrument. All other measurements were performed at room temperature. Zeta potential measurements were carried out on a Malvern Zetasizer Nano instrument equipped with a 4.0 mW He–Ne laser operating at λ = 633 nm.

Results and discussion

Phase analysis

The crystal structure and phase purity of the samples were characterized by PXRD. Fig. 1(a) shows the PXRD pattern of the MoS_2 sample prepared *via* the hydrothermal route and can be readily indexed to the hexagonal phase of MoS_2, which is consistent with the standard powder diffraction pattern of MoS_2 (JCPDS 37-1492) shown in Fig. 1(b). The typical XRD patterns of the MoS_2–$NaYF_4$:Yb^{3+}/Er^{3+} nanocomposites and $NaYF_4$:Yb^{3+}/Er^{3+} NCs are shown in Fig. 1(c and d), respectively. For $NaYF_4$:Yb^{3+}/Er^{3+} NCs, the diffraction peaks were well-defined, and the peak positions and intensities agreed well with the standard cubic pattern of $NaYF_4$ (PDF card no. 01-077-2042) shown in Fig. 1(e), indicating that the as-prepared $NaYF_4$:Yb^{3+}/Er^{3+} NCs material is pure and crystallizes in the cubic phase. Fig. 1(c) shows the XRD pattern of MoS_2–$NaYF_4$:Yb^{3+}/Er^{3+} nanocomposites obtained *via* a one-pot hydrothermal route. The sample shows the characteristic peaks of $NaYF_4$:Yb^{3+}/Er^{3+} NCs, but it is worth mentioning the appearance of a weak diffraction peak (see Fig. 1c) at 2θ = 14.4°. This peak is assigned to the (002) plane of MoS_2, which supports the presence of MoS_2 in MoS_2–$NaYF_4$:Yb^{3+}/Er^{3+} nanocomposites. The weak intensity of the MoS_2 peaks is due to the presence of small amounts of MoS_2 in the nanocomposites.

Morphology analysis

High resolution scanning electron microscopy was used for morphology and size analysis of the as-synthesized samples. FE-SEM images shown in Fig. 2(a) illustrate that the adipic acid capped $NaYF_4$:Yb^{3+}/Er^{3+} NCs are spherical in morphology. The average particle size of the $NaYF_4$:Yb^{3+}/Er^{3+} NCs is approximately 40 nm. The SEM images of MoS_2 shown in Fig. 2(b) indicate the formation of a cauliflower-like morphology. At a

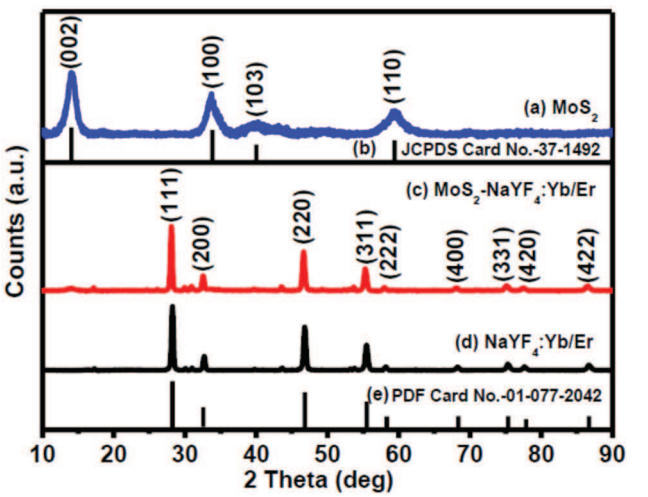

Fig. 1 XRD patterns of (a) MoS_2, (c) MoS_2–$NaYF_4$:Yb^{3+}/Er^{3+} (d) $NaYF_4$:Yb^{3+}/Er^{3+} nanomaterials and (b and e) standard XRD patterns of MoS_2 and bulk $NaYF_4$.

Published on 04 July 2016. Downloaded by Monash University on 19/07/2016 03:34:49.

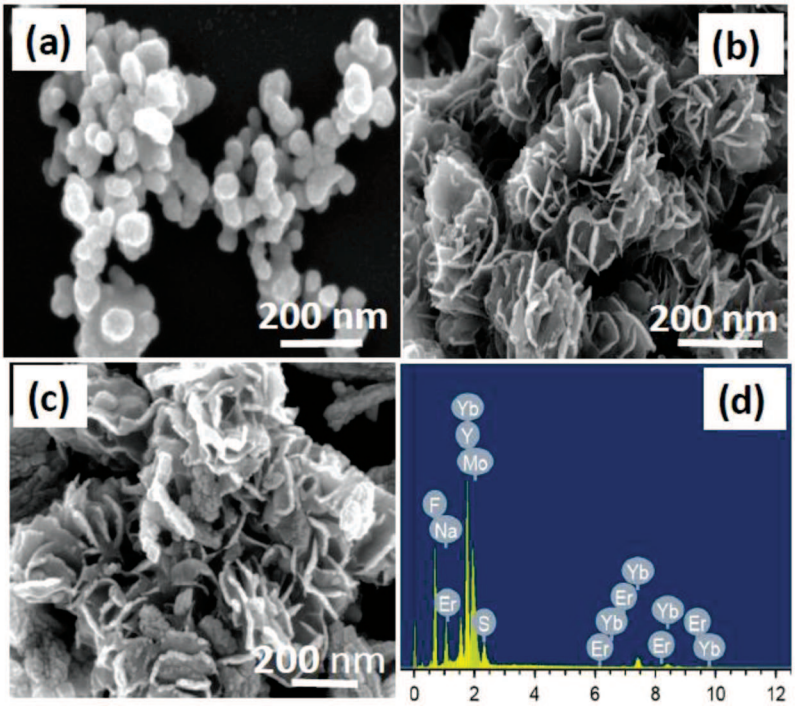

Fig. 2 FE-SEM images of (a) $NaYF_4$:Yb^{3+}/Er^{3+} NCs, (b) MoS_2 and (c) MoS_2–$NaYF_4$:Yb^{3+}/Er^{3+} nanocomposites. EDX spectrum of (d) MoS_2–$NaYF_4$:Yb^{3+}/Er^{3+} nanocomposites.

closer look it is clear that the MoS_2 nanostructure is composed of nanowalls of about several nanometers in thickness.[45] For the MoS_2–$NaYF_4$:Yb^{3+}/Er^{3+} nanocomposites, changes in the roughness of MoS_2 nanostructures upon deposition of $NaYF_4$ nanocrystals on MoS_2 nanostructures can be clearly observed in the FESEM images shown in Fig. 2(c). We believe that during the initial growth of the nanocomposite, the cations attach onto the negatively charged MoS_2 nanosheets through electrostatic interactions. This presumption is supported by the observed zeta potential value of −19 mV for MoS_2 nanosheets. The nanosheets then act as a nucleation site for the growth of the NCs. This suggests the successful formation of the MoS_2–$NaYF_4$:Yb^{3+}/Er^{3+} nanocomposites. The EDX spectral results shown in Fig. 2(d) further confirm the presence of elements (such as Mo, S, Na, Y, F, Yb and Er) in the nanocomposites. The photoluminescence measurements of the resulting products provide further evidence for the formation of MoS_2–$NaYF_4$:Yb^{3+}/Er^{3+} composites (*vide infra*).

Surface functionalization-FTIR analysis

The attachment of adipic acid molecules onto the surface of the nanocrystals is confirmed from Fourier transform infrared (FTIR) analysis. The FTIR spectra of adipic acid capped $NaYF_4$:Yb^{3+}/Er^{3+} NCs and MoS_2–$NaYF_4$:Yb^{3+}/Er^{3+} nanocomposites along with pure adipic acid are shown in Fig. S1.† All the IR absorption bands of the main functional groups present in the adipic acid are observed. In the case of $NaYF_4$ nanocrystals and MoS_2–$NaYF_4$:Yb^{3+}/Er^{3+} nanocomposites a weak peak near 1565 cm^{-1} due to carbonyl stretching is observed. This stretching frequency is much lower than the 1708 cm^{-1} observed for the free adipic acid molecules, implying the binding of the O-atom of the –COOH group of adipic acid to the surface of the nanocrystals. The binding of adipic acid molecules to the nanocrystals makes the surface of the nanocrystals hydrophilic, to disperse them in polar solvents.

UV-vis-NIR absorption properties

Fig. 3 shows the UV-Vis spectrum of MoS_2. Three absorption peaks at 450, 624 and 670 nm are observed for MoS_2, which show the semiconducting nature of MoS_2. The two characteristic absorption peaks at 624 nm (1.99 eV) and 670 nm (1.85 eV) arise from direct transition from valence band to conduction band at the *K*-point of the Brillouin zone, known as the B and A transitions, respectively. The small energy difference between the two peaks is a result of the spin–orbital splitting of the valence band. In addition, a broad absorption band centered at 450 nm (2.75 eV) arising from the complicated C and D transitions is also observed.[46–50] In the inset of Fig. 4—the absorption spectra of (a) MoS_2–$NaYF_4$:Yb^{3+}/Er^{3+} nanocomposites and (b) pure $NaYF_4$:Yb^{3+}/Er^{3+} NCs—the characteristic absorption peaks between 400 and 700 nm corresponding to MoS_2 are observed. The observed weak UV-Vis absorption of MoS_2 in the nanocomposites is due to the low amount of MoS_2 loading.

Upconversion (UC) luminescence properties

The UC emission spectrum of adipic acid encapsulated Yb^{3+}(20%)/Er^{3+}(2%)-doped $NaYF_4$ NCs upon excitation with a

This journal is © The Royal Society of Chemistry 2016

Published on 04 July 2016. Downloaded by Monash University on 19/07/2016 03:34:49.

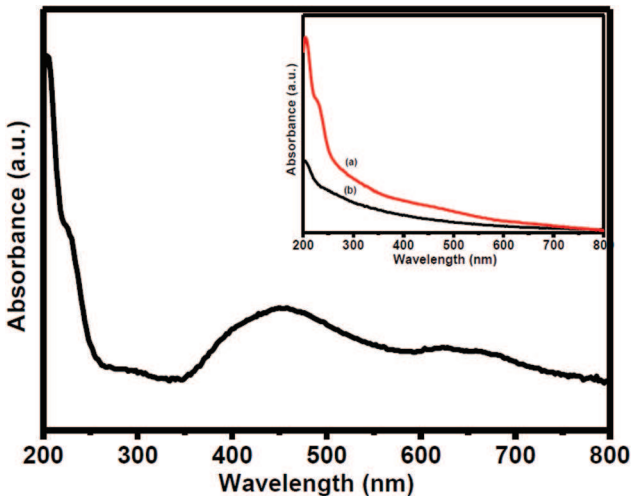

Fig. 3 UV-Vis absorption spectrum of MoS_2. Inset shows the UV-Vis absorption spectra of (a) MoS_2–$NaYF_4$:Yb^{3+}/Er^{3+} nanocomposite (red curve) and (b) $NaYF_4$:Yb^{3+}/Er^{3+} (black curve).

980 nm continuous wave (CW) diode laser is shown in Fig. 4(a), where Yb^{3+} serves as a sensitizer and Er^{3+} acts as an activator. Four major bands are observed around 408, 523 nm, 545 nm, and 655 nm in the UC emission spectrum. The intense green emissions appearing close to 520 and 545 nm are assigned to the $^2H_{11/2} \rightarrow {}^4I_{15/2}$ and $^4S_{3/2} \rightarrow {}^4I_{15/2}$ transitions in Er^{3+}, respectively. The strong emission peak appearing in the red region is assigned to a transition occurring between the $^4F_{9/2}$ and $^4I_{15/2}$ levels of Er^{3+}. The violet emission (408 nm) and UV emission (379 nm) are ascribed to the $^2H_{9/2} \rightarrow {}^4I_{15/2}$ and $^4G_{11/2} \rightarrow {}^4I_{15/2}$ transitions of Er^{3+} ions, respectively. The involvement of two 980 nm photons in providing both green and red emission is verified by performing power-dependent studies, as the UC emission intensity (I) is directly proportional to the n^{th} power of the laser power (P), $I \propto P^n$. A plot of ln(I) *versus* ln(P) for both green and red emissions of the $NaYF_4$:Yb^{3+}/Er^{3+} NCs along with the resulting slope values are shown in Fig. S2.† The calculated values are 1.58 and 1.33 for 545 nm and 650 nm emissions of $NaYF_4$:Yb^{3+}/Er^{3+} NCs, respectively. The above values clearly suggest the participation of two 980 nm photons in producing both green and red emissions. These values are lower than the expected value of 2 due to saturation of the UC process.[51] The possible energy transfer mechanism between Yb^{3+} and Er^{3+} is shown in Fig. S3,† using the energy level diagram of Yb^{3+} and Er^{3+} ions. Fig. 4(c) indicates a drastic decrease in the observed upconversion emission intensity for MoS_2–$NaYF_4$:Yb^{3+}/Er^{3+} nanocomposites. We believe this strong quenching of the upconverted fluorescence of $NaYF_4$:Yb^{3+}/Er^{3+} NCs is likely to be due to MoS_2. This is reasonable because MoS_2 has strong absorption over a wide wavelength region (350 to 700 nm), as shown in Fig. 3. This covers the fluorescence emission regions of $NaYF_4$:Yb^{3+}/Er^{3+} NCs. In order to understand whether the reduction in the UC luminescence intensity is due to energy transfer or instead due to radiation–reabsorption, we performed a control experiment. A physical mixture of MoS_2 and $NaYF_4$:Yb^{3+}/Er^{3+} NCs was prepared by taking the same molar ratio as that in the nanocomposite. The mixture was ground well and its UC properties were studied. The mixture shows intense UC upon excitation at 980 nm and the extent of reduction in the upconversion emission intensity is much less compared to that noted for the nanocomposites. This suggests that the observed decrease in the intensity of the UC emission for the nanocomposites is likely to be due to high energy transfer from the excited Er^{3+} ions to MoS_2 in the nanocomposites. To further understand the quenching mechanism, lifetime measurements were performed (as shown in Fig. S4†). The lifetime curves were obtained by the direct excitation of the Er^{3+} ions at an excitation wavelength of 488 nm. The significant decrease in the decay time of Er^{3+} ions in nanocomposites (8 μs) compared to that in the $NaYF_4$:Yb^{3+}/Er^{3+} NCs alone (40 μs) indicates that the energy migration between $NaYF_4$:Yb^{3+}/Er^{3+} NCs and MoS_2 is a resonance energy transfer (RET) process, rather than a radiation–reabsorption process or charge transfer process. The latter is a difficult process, as the redox potentials of many of the lanthanide ions are high. In particular, it is worth mentioning that the difference in the energy transfer efficiency from Er^{3+} to MoS_2 affects the NIR photocatalytic activity of MoS_2 significantly, which will be discussed in the photocatalytic activity section (*vide infra*).

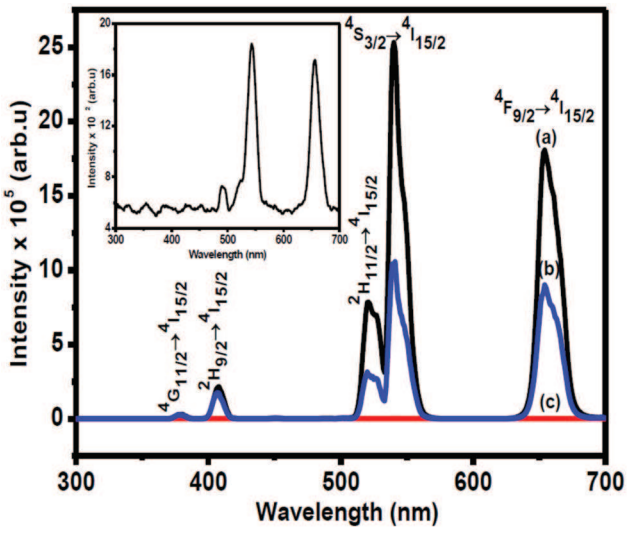

Fig. 4 The UC emission spectra of (a) $NaYF_4$:Yb^{3+}/Er^{3+} NCs, (b) physical mixture of $NaYF_4$:Yb^{3+}/Er^{3+} NCs and MoS_2 and (c) MoS_2–$NaYF_4$:Yb^{3+}/Er^{3+} composites (magnified spectrum shown in the inset) under 980 nm excitation.

Photocatalytic study

The photocatalytic performance of the MoS_2–$NaYF_4$:Yb^{3+}/Er^{3+} nanocomposites was evaluated by studying the degradation of Rhodamine B (RhB) dye under 980 nm NIR irradiation. 20 mg of the MoS_2–$NaYF_4$:Yb^{3+}/Er^{3+} nanocomposites were dispersed into a quartz vial containing 10 mL of RhB aqueous solution. In order to determine the actual amount of RhB decomposed

Published on 04 July 2016. Downloaded by Monash University on 19/07/2016 03:34:49.

via photocatalysis, a dark reaction of RhB in the presence of catalysts was conducted to establish the adsorption/desorption equilibrium of RhB on the surfaces of the MoS_2–$NaYF_4$:Yb^{3+}/Er^{3+} nanocomposites. As can be seen from Fig. 5, the nanocomposite adsorbs about 37.5% of RhB after 1 hour in dark conditions. Thereafter, the solution was subjected to NIR irradiation and 1 mL of RhB aqueous solution was taken out for UV-vis absorption measurement after regular intervals of 1 hour. This high adsorption of dye molecules on the composite photocatalyst may be ascribed to the 2D nature of the MoS_2 nanosheets. In comparison to nanoparticles, 2D nanosheets are known to possess a large surface area, which in turn is able to adsorb significantly more dye molecules than nanoparticles. Moreover, the photocatalytic activity of a material depends largely on the extent of adsorption by the photocatalyst. Hence, both high adsorption and large surface area also assist in the photocatalysis process. We believe that the nature of the adsorption of pollutants on photocatalyst surfaces follows Langmuir's theory, which postulates that adsorption is monolayered and excess molecules are reflected back from the surfaces.[52] It was earlier reported that photogenerated oxidizing species are not able to migrate far from the photocatalysts and the degradation process occurs at the surface or within a few monolayers around the photocatalytic particles.[53]

Fig. 5 shows the absorbance spectra of RhB-loaded MoS_2–$NaYF_4$:Yb^{3+}/Er^{3+} nanocomposites under NIR irradiation as a function of irradiation time. The observed gradual decrease in the absorption intensity of RhB at 554 nm with an increase in irradiation time clearly indicates the degradation of RhB upon NIR irradiation. Fig. 6 shows the time-dependent profile of C/C_0 (degradation ratio), where C is the concentration of RhB irradiated with a 980 nm laser for time t and C_0 is the original concentration of RhB after attaining adsorption equilibrium with the photocatalysts well before irradiation. From Fig. 6, it is clear that the degradation ratio (C/C_0) of RhB was observed to increase continuously with irradiation time and reached about 61% after 12 h irradiation in the presence of MoS_2–$NaYF_4$:Yb^{3+}/Er^{3+} nanocomposites. The observed degradation rate is much higher than the rate for other upconversion photocatalysts (see Table S1 in ESI†). We strongly believe the observed faster degradation is due to the layered nature of MoS_2 and the excellent upconversion properties of NCs. The surface area of a photocatalyst plays an important role behind its activity. Thus, BET surface area measurements were carried out, which clearly indicate there is not much change in the surface area of MoS_2 in the composite (10.74 $m^2\ g^{-1}$) upon deposition of $NaYF_4$:Yb^{3+}/Er^{3+} NCs compared to MoS_2 alone (13.78 $m^2\ g^{-1}$). Furthermore, to study the difference in the photocatalytic ability of MoS_2–$NaYF_4$:Yb^{3+}/Er^{3+} nanocomposites and the $NaYF_4$-Yb/Er/MoS_2 physical mixture, the latter was mixed with RhB solution and irradiated with NIR light for 12 h. Interestingly, only 18% of the RhB was found to be decomposed, which is almost three times lower than that observed for MoS_2–$NaYF_4$:Yb^{3+}/Er^{3+} nanocomposites (61%). We attribute this to the difference in their energy migration pathways, as was discussed in the upconversion section. In the nanocomposites structure, $NaYF_4$:Yb^{3+}/Er^{3+} NCs and MoS_2 are attached closely to each other and form compact interfaces. This benefits energy transfer processes, as the distances between MoS_2 and UC nanoparticles are within the energy transfer distance. In contrast, we believe there are no contact interfaces between $NaYF_4$-Yb/Er and MoS_2 nanomaterials in the physical mixture, and thus, MoS_2 can be excited mainly *via* radiation–reabsorption. However, in the MoS_2–$NaYF_4$:Yb^{3+}/Er^{3+} nanocomposites, more NIR photon energy has been used to activate MoS_2, leading to relatively higher photocatalytic activity. These results indicate that energy transfer is an important mechanism in the NIR photocatalytic activity. Moreover, $NaYF_4$:Yb^{3+}/Er^{3+} NCs and MoS_2 alone showed limited

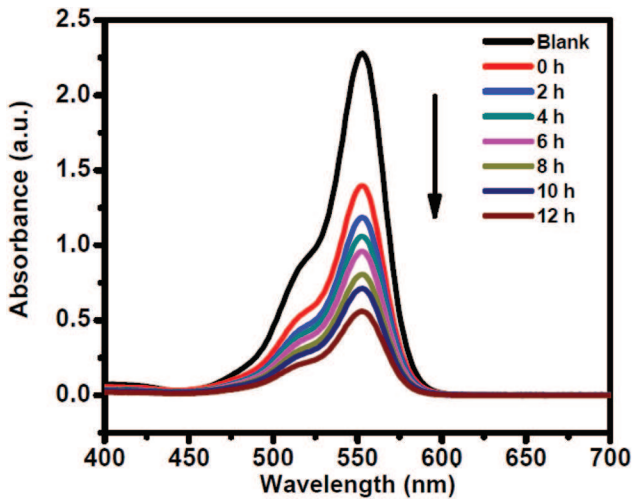

Fig. 5 Temporal evolution of the absorbance spectra of RhB degradation under NIR irradiation in the presence of MoS_2–$NaYF_4$:Yb^{3+}/Er^{3+} nanocomposites.

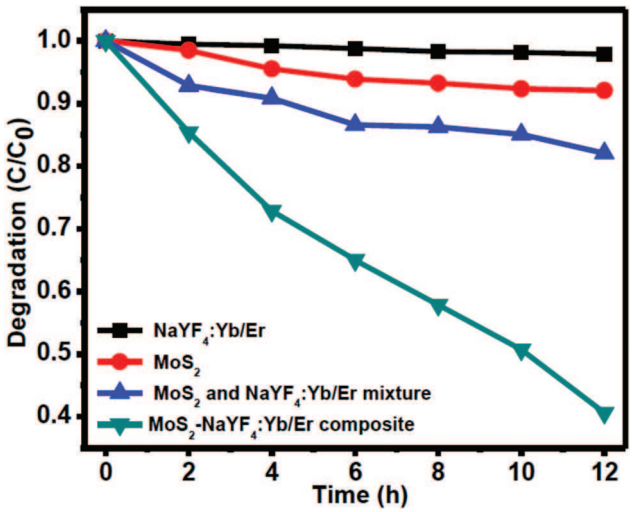

Fig. 6 The photocatalytic degradation rates of RhB under NIR irradiation for different photocatalyst solutions.

This journal is © The Royal Society of Chemistry 2016

Published on 04 July 2016. Downloaded by Monash University on 19/07/2016 03:34:49.

photocatalytic activities for degradation of RhB. It is also well established in the literature that the thermal energy generated by NIR irradiation is not sufficient to induce the thermal degradation of RhB.[41]

It is essential to understand the origin of the degradation of RhB under irradiation by a 980 nm NIR laser in the presence of MoS_2–$NaYF_4$:Yb^{3+}/Er^{3+} nanocomposites. In most cases, it is reactive oxygen species like hydroxyl radicals ($^{\bullet}OH$) that are considered to be responsible for the degradation of organic contaminants because of their strong oxidation ability. To confirm the generation of $^{\bullet}OH$ during the photocatalytic process of MoS_2–$NaYF_4$:Yb^{3+}/Er^{3+} nanocomposites under NIR irradiation, we used terephthalic acid (TA) as a fluorescence probe to measure $^{\bullet}OH$ generation. The nonfluorescent TA captures $^{\bullet}OH$ to form hydroxyterephthalic acid (TAOH), which shows fluorescence at 424 nm upon excitation with 312 nm UV light. Therefore, the formation of TAOH as well as the generation of $^{\bullet}OH$ can be selectively detected by monitoring the emission intensity at 424 nm. Fig. 7(a) shows photoluminescence spectra for the supernatant solution of the photocatalyst suspension containing 4 mM TA irradiated with a 980 nm NIR laser for a designated time. The collected spectra are characteristic of the fluorescence of TAOH, which indicates that $^{\bullet}OH$ is being produced during the NIR photocatalytic reactions. Moreover, the increased intensity with irradiation time indicates an increase in $^{\bullet}OH$ generation. Fig. 7(b) shows the time-dependent evolution of the fluorescence intensity of TAOH in the presence of different photocatalysts. The rate of generation of $^{\bullet}OH$ can be evaluated by the slope of the curve in Fig. 7(b). It is clear from this figure that upon NIR irradiation, almost no $^{\bullet}OH$ was generated in the case of MoS_2 and $NaYF_4$:Yb^{3+}/Er^{3+} NCs alone, suggesting that hardly any degradation of organic species occurs in the presence of these materials. On the other hand, in the presence of MoS_2–$NaYF_4$:Yb^{3+}/Er^{3+} composites, $^{\bullet}OH$ radicals were produced upon NIR irradiation. These results indicate that the energy transfer efficiency between $NaYF_4$:Yb^{3+}/Er^{3+} NCs and MoS_2 is the key to the cause of the NIR photocatalytic activity.

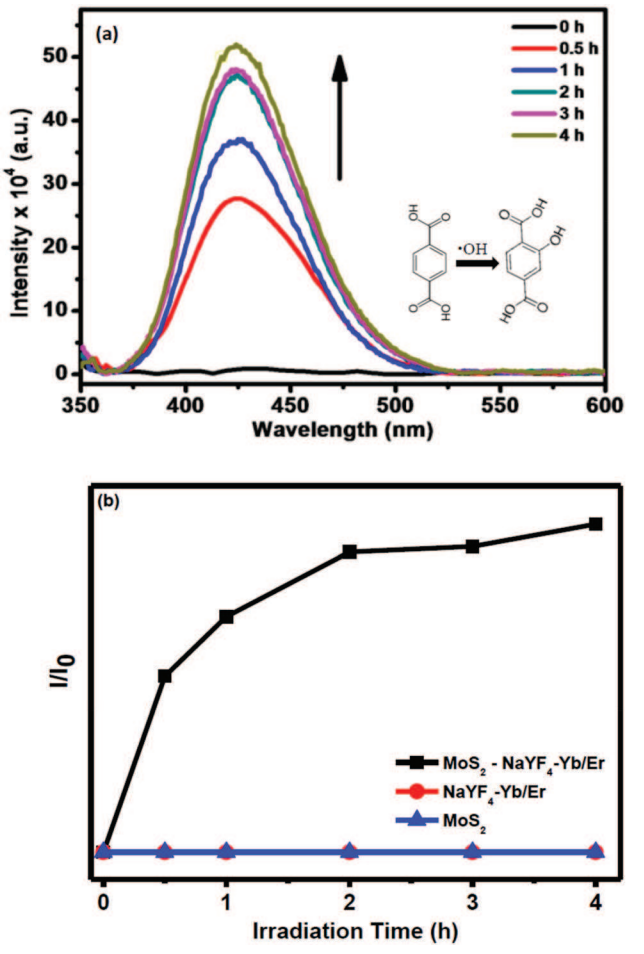

Fig. 7 (a) Emission spectra of terepthalic acid (TA) solution and (b) fluorescence intensity ratio of the emission peak of TAOH at 420 nm as a function of time upon irradiation with a 980 nm laser in the presence of MoS_2–$NaYF_4$-Yb/Er nanocomposites.

Photocatalysis mechanism

Scheme 1 describes the overall processes involved in the photocatalysis by the MoS_2–$NaYF_4$:Yb^{3+}/Er^{3+} nanocomposites under irradiation by a 980 nm NIR laser. It involves three main processes: (1) the formation of the excited states of Er^{3+}, (2) the activation of the semiconductor *via* energy transfer, and (3) the generation of reactive oxygen species. Upon 980 nm excitation, the higher energy levels of the Er^{3+} ions ($^4I_{11/2}$, $^4F_{9/2}$ and $^4H_{9/2}$) are populated *via* a successive energy transfer processes from Yb^{3+} to Er^{3+}. The semiconductor MoS_2 is excited by the energy transfer from upconverting luminescent $NaYF_4$:Yb^{3+}/Er^{3+} NCs. Thus, MoS_2 is activated to produce photogenerated carriers: that is, electrons and holes in the conduction band (CB) and the valence band (VB), respectively (see Scheme 1). These electron–hole pairs migrate from the inner region to the surface to take part in surface reactions. As shown in Scheme 1, the excited electrons arriving on the surface react with the oxygen adsorbed on the surface of MoS_2 to form superoxide radical

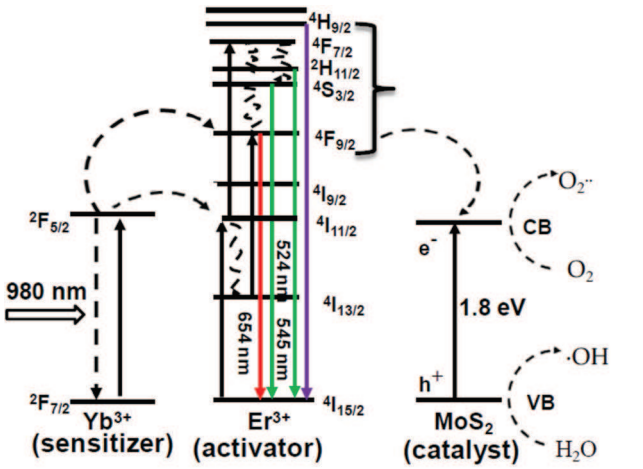

Scheme 1 Schematic illustration of near-infrared activated photocatalysis in MoS_2–$NaYF_4$:Yb^{3+}/Er^{3+} nanocomposites.

Published on 04 July 2016. Downloaded by Monash University on 19/07/2016 03:34:49.

anions ($O_2^{\bullet-}$), whereas the photogenerated strongly oxidative holes (h^+) react with H_2O to produce hydroxyl radicals ($^{\bullet}OH$), a process which is considered to be the main contributor to the degradation of RhB dye.

Conclusions

In summary, adipic acid encapsulated $NaYF_4$:Yb^{3+}/Er^{3+} upconversion nanocrystals were synthesized successfully by a hydrothermal method. The as-synthesized NCs possess strong UC emission in the visible and UV regions of the solar spectrum. The potential for UC nanocrystals to absorb NIR light in the solar spectrum is utilized to enhance the photocatalytic performance of MoS_2. The strong NIR-driven photocatalytic capability of a MoS_2–$NaYF_4$-Yb^{3+}/Er^{3+} upconversion photocatalyst is demonstrated *via* the degradation of RhB dye. Further, comparative studies performed between the MoS_2–$NaYF_4$:Yb^{3+}/Er^{3+} composites and the physical mixture of MoS_2 and $NaYF_4$:Yb^{3+}/Er^{3+} NCs revealed the presence of different energy transfer pathways in the nanocomposites and the mixture, which resulted in a large difference in the NIR-driven photocatalytic activities. In addition, a series of control experiments revealed that the hydroxyl radicals are responsible for Rhodamine B (RhB) dye degradation under NIR irradiation. In conclusion, we have developed a facile method to synthesize MoS_2–$NaYF_4$:Yb^{3+}/Er^{3+} nanocomposites that combines the advantages of both MoS_2 and upconversion nanoparticles which can be used for applications beyond photocatalysis, such as for broadband optical limiting applications or optoelectronic devices.

Acknowledgements

VM thanks the Department of Science and Technology (DST) India, CSIR and IISER-Kolkata for the funding. MC thanks KVPY for his scholarship. VNKBA and SG thank UGC and CSIR, respectively, for their scholarship.

References

1 X. Bai, L. Wang, R. Zong, Y. Lv, Y. Sun and Y. Zhu, *Langmuir*, 2013, **29**, 3097–3105.
2 W. Yao, B. Zhang, C. Huang, C. Ma, X. Song and Q. Xu, *J. Mater. Chem.*, 2012, **22**, 4050–4055.
3 S. Higashimoto, Y. Tanaka, R. Ishikawa, S. Hasegawa, M. Azuma, H. Ohue and Y. Sakata, *Catal. Sci. Technol.*, 2013, **3**, 400–403.
4 Y. Wang, Z. Wang, S. Muhammad and J. He, *CrystEngComm*, 2012, **14**, 5065–5070.
5 Z. Ai, L. Zhang, S. Lee and W. Ho, *J. Phys. Chem. C*, 2009, **113**, 20896–20902.
6 X. J. Liu, L. K. Pan, T. Lv, Z. Sun and C. Q. Sun, *J. Colloid Interface Sci.*, 2013, **408**, 145–150.
7 X. J. Liu, L. K. Pan, T. Lv, T. Lu, G. Zhu, Z. Sun and C. Q. Sun, Microwave-assisted synthesis of ZnO–graphene composite for photocatalytic reduction of Cr(VI), *Catal. Sci. Technol.*, 2011, **1**, 1189–1193.
8 T. Kamegawa, S. Matsuura, H. Seto and H. Yamashita, *Angew. Chem., Int. Ed.*, 2013, **52**, 916–919.
9 W. P. Qin, D. S. Zhang, D. Zhao, L. L. Wang and K. Z. Zheng, *Chem. Commun.*, 2010, **46**, 2304–2306.
10 M. Anpo and M. Takeuchi, *Int. J. Photoenergy*, 2001, **3**, 89–94.
11 M. A. Grela and J. A. Colussi, *J. Phys. Chem.*, 1996, **100**, 18214–18221.
12 G. K. Mor, K. Shankar, M. Paulose and C. A. Grimes, *Nano Lett.*, 2005, **5**, 191–195.
13 B. Luo, G. Liu and L. Wang, *Nanoscale*, 2016, **13**(8), 6904–6920.
14 F. Dong, L. Wu, Y. Sun, M. Fu, Z. Wu and S. C. Lee, *J. Mater. Chem.*, 2011, **21**, 15171.
15 J. Hong, Y. Wang, W. Zhang and R. Xu, *ChemSusChem*, 2013, **6**, 2263–2268.
16 Y. P. Venkata Subbaiah, K. K. J. J. Saji and A. Tiwari, *Adv. Funct. Mater.*, 2016, **26**(13), 2046–2069.
17 M. Chhowalla, H. S. Shin, G. Eda, L.-J. Li, K. P. Loh and H. Zhang, *Nat. Chem.*, 2013, **5**, 263–275.
18 C. Tana and H. Zhang, *Chem. Soc. Rev.*, 2015, **44**, 2713–2731.
19 J. Kibsgaard, Z. Chen, B. N. Reinecke and T. F. Jaramillo, *Nat. Mater.*, 2012, **11**, 963–969.
20 J. Li, K. Yu, Y. Tan, H. Fu, Q. Zhang, W. Cong, C. Song, H. Yin and Z. Zhu, *Dalton Trans.*, 2014, **43**, 13136–13144.
21 F. A. Frame and F. E. Osterloh, *J. Phys. Chem. C*, 2010, **114**, 10628–10633.
22 L. A. King, W. Zhao, M. Chhowalla, D. J. Riley and G. Eda, *J. Mater. Chem. A*, 2013, **1**, 8935–8941.
23 Y. Li, Y. Li, C. M. Araujo, W. Luo and R. Ahuja, *Catal. Sci. Technol.*, 2013, **3**, 2214–2220.
24 B. Visic, R. Dominko, M. K. Gunde, N. Hauptman, S. D. Skapin and M. Remskar, *Nanoscale Res. Lett.*, 2011, **6**, 1–6.
25 S. Sivakumar, F. C. J. M. van Veggel and P. S. May, *J. Am. Chem. Soc.*, 2007, **129**, 620–625.
26 F. Wang, X. J. Xue and X. Liu, *Angew. Chem., Int. Ed.*, 2008, **47**, 906–909.
27 F. Wang, Y. Han, C. S. Lim, Y. Lu, J. Wang, J. Xu, H. Chen, C. Zhang, M. Hong and X. Liu, *Nature*, 2010, **463**, 1061–1065.
28 M. Haase and H. Schäfer, *Angew. Chem., Int. Ed.*, 2011, **50**, 5808–5829.
29 O. Ehlert, R. Thomann, M. Darbandi and T. Nann, *ACS Nano*, 2008, **2**, 120–124.
30 J.-C. G. Bünzli, *Chem. Rev.*, 2010, **110**, 2729–2755.
31 X. Zhang, P. Yang, Y. Dai, P. Ma, X. Li, Z. Cheng, Z. Hou, X. Kang, C. Li and J. Lin, *Adv. Funct. Mater.*, 2013, **23**, 4067–4078.
32 J. de Wild, A. Meijerink, J. K. Rath, W. G. J. H. M. van Sark and R. E. I. Schropp, *Energy Environ. Sci.*, 2011, **4**, 4835–4848.
33 S. Sarkar, B. Meeseragandla, C. Hazra and V. Mahalingam, *Adv. Mater.*, 2013, **25**, 856–860.

 This journal is © The Royal Society of Chemistry 2016

Published on 04 July 2016. Downloaded by Monash University on 19/07/2016 03:34:49.

34 C. Boyer, F. Vetrone, L. A. Cuccia and J. A. Capobianco, *J. Am. Chem. Soc.*, 2006, **128**, 7444–7445.
35 D. K. Chatterjee, M. K. Gnanasammandhan and Y. Zhang, *Small*, 2010, **6**, 2781–2795.
36 M. Quintanilla, I. X. Cantarelli, M. Pedroni, A. Speghini and F. Vetrone, *J. Mater. Chem. C*, 2015, **3**, 3108–3113.
37 J. C. Boyer, N. J. J. Johnson and F. C. J. M. van Veggel, *Chem. Mater.*, 2009, **21**, 2010–2012.
38 W. Qin, D. Zhang, D. Zhao, L. Wanga and K. Zhenga, *Chem. Commun.*, 2010, **46**, 2304–2306.
39 Y. Tang, W. Di, X. Zhai, R. Yang and W. Qin, *ACS Catal.*, 2013, **3**, 405–412.
40 X. Guo, W. Song, C. Chen, W. Di and W. Qin, *Phys. Chem. Chem. Phys.*, 2013, **15**, 14681–14688.
41 C. Li, F. Wang, J. Zhu and J. C. Yu, *Appl. Catal., B*, 2010, **100**, 433–449.
42 X. Guo, W. Di, C. Chen, C. Liu, X. Wang and W. Qin, *Dalton Trans.*, 2014, **43**, 1048–1054.
43 Q. C. Xu, Y. Zhang, M. J. Tan, Y. Liu, S. Yuan, C. Choong, N. S. Tan and T. T. Y. Tan, *Adv. Healthcare Mater.*, 2012, **1**, 470–474.
44 M.-Z. Huang, B. Yuan, L. Dai and M.-L. Fu, *J. Colloid Interface Sci.*, 2015, **460**, 264–272.
45 M. Chhowalla, H. S. Shin, G. Eda, L.-J. Li, K. P. Loh and H. Zhang, *Nat. Chem.*, 2013, **5**, 263–275.
46 K. F. Mak, K. He, C. Lee, G. H. Lee, J. Hone, T. F. Heinz and J. Shan, *Nat. Mater.*, 2013, **12**, 207–211.
47 A. Splendiani, L. Sun, Y. Zhang, T. Li, J. Kim, C.-Y. Chim, G. Galli and F. Wang, *Nano Lett.*, 2010, **10**, 1271–1275.
48 N. Bogdan, F. Vetrone, G. A. Ozin and J. A. Capobianco, *Nano Lett.*, 2011, **11**, 835–840.
49 G. Eda, H. Yamaguchi, D. Voiry, T. Fujita, M. Chen and M. Chhowalla, *Nano Lett.*, 2011, **11**, 5111–5116.
50 A. O'Neill, U. Khan and J. N. Coleman, *Chem. Mater.*, 2012, **24**, 2414–2421.
51 M. Pollnau, D. R. Gamelin, S. R. Luthi, H. U. Gudel and M. P. Hehlen, *Phys. Rev. B: Condens. Matter*, 2000, **61**, 3337–3346.
52 U. Gaya, *Heterogeneous photocatalysis using Inorganic semiconductor solids*, 2013, p. 75, section 3.2.
53 C. Minero, F. Catozzo and E. Pelizzetti, *Langmuir*, 1992, **8**, 481–486.